Full Length Article

Tunable electronic and magnetic properties of MoSi$_2$N$_4$ monolayer via vacancy defects, atomic adsorption and atomic doping

A. Bafekry [a,b,*], M. Faraji [c], Mohamed M. Fadlallah [d], A. Bagheri Khatibani [e], A. abdolahzadeh Ziabari [e], M. Ghergherehchi [f,*], Sh. Nedaei [g], S. Farjami Shayesteh [g], D. Gogova [h]

[a] Department of Radiation Application, Shahid Beheshti University, Tehran 1983969411, Iran
[b] Department of Physics, University of Antwerp, Groenenborgerlaan 171, B-2020 Antwerp, Belgium
[c] Micro and Nanotechnology Graduate Program, TOBB University of Economics and Technology, Sogutozu Caddesi No 43 Sogutozu, 06560 Ankara, Turkey
[d] Department of Physics, Faculty of Science, Benha University, 13518 Benha, Egypt
[e] Nano Research Lab, Lahijan Branch, Islamic Azad University, Lahijan, Iran
[f] College of Electronic and Electrical Engineering, Sungkyunkwan University, Suwon, South Korea
[g] Department of Physics, University of Guilan, 41335-1914 Rasht, Iran
[h] Center for Materials Science and Nanotechnology, University of Oslo, Oslo, Norway

A R T I C L E I N F O

A B S T R A C T

The two dimensional MoSi$_2$N$_4$ (MSN) monolayer exhibiting rich physical and chemical properties was synthesized for the first time last year. We have used the spin-polarized density functional theory to study the effect of different types of point defects on the structural, electronic, and magnetic properties of the MSN monolayer. Adsorbed, substitutionally doped (at different lattice sites), and some kind of vacancies have been considered as point defects. The computational results show all defects studied decrease the MSN monolayer band gap. We found out the H-, O-, and P-doped MSN are n-type conductors. The arsenic-doped MSN, and MSN with vacancy defects have a magnetic moment. The MSN with a Si vacancy defect is a half-metallic which is favorable for spintronic applications, while the MSN with a single N vacancy or double vacancy (N + S) defects are metallic, i. e., beneficial as spin filters and chemical sensors.

1. Introduction

Two-dimensional materials (2DMs) are the most fascinating materials nowadays due to their amazing properties and tempting potential applications [1]. Since 2004 when the first 2DM - graphene - has been discovered many other two-dimensional crystals have been exfoliated from different layered materials [2]. The 2DMs have demonstrated real and potential optical, electrical, mechanical, thermoelectrical, catalytic, energy conversion and storage, spintronic, photonics, etc. applications [3–9]. 2DMs-based devices exhibit outstanding characteristics with appropriate optical gain, controllable spectrum sensitivity, large photoresponse bandwidth, and acceptable conversion efficiency [10]. They belong to a wide range of materials with diverse chemical compositions and various properties that may be rather different from their bulk counterparts [11]. Easy modification of the 2DMs properties by nano design makes various nanostructures to manifest insulating,

semiconducting, half-metallic, metallic, and even superconducting properties [12–16]. In modern electronics, there is a necessity for ultrathin materials and hence, the 2DMs are ready to be used effectively [16].

Defects exist in all real materials and influence their properties such as electrical, magnetic, mechanical, and so on [16,17]. Defects have been widely investigated from different points of view. For example, as a category of catalytic active sites, because of their high distortion energy and different arrangements of the atoms compared to regular crystalline structures [18]. In conventional materials, studying the defects is comprehensively developed and there is a huge amount of related papers, however, this is not the case of the 2DMs [19]. Obviously, the effect of defects and their variation inside the low-dimensional materials should be investigated in detail, even though, defect engineering in the 2DMs has been the subject of major research in recent years [20–23]. Common defects such as the monovacancy, divacancy, Stone Wales

[24–26], antisite, substitution, adatom, heterostructures [27], charged impurities [28–30], and grain boundary have been observed in the 2DMs [31,32]. They have a larger impact on the electronic and optical properties of 2D materials [33–35]. Defects can play different roles such as carrier donors, scattering, trapping, and recombination centers [36–39]. Furthermore, the properties of the 2DMs can be tailored via defect engineering [40–43].

For example, the chemical doping by substitution of foreign atoms, and the making of specific vacancies or divacancies can create localized or resonance states inside the band gap [44]. Furthermore, at low concentration of point defects, a slight coupling occurs between adjacent defects and leads to localized states and magnetic moments. Also, lattice distortions (e.g. cracks and large voids) give rise to localized states at the Fermi level and create magnetic moments [45,46]. In addition to the defects, the 2DMs can tolerate different strains before reaching a rupture and may be stretched because of having plastic properties. Thus, strain engineering has received considerable attention to regulate the desired performance in various applications [47–49]. It was reported that nanoscale local strains alter the fundamental band gap and modify the electromagnetic properties of monolayered 2DMs. Besides that, applying biaxial strain can change the non-magnetic monolayered 2DMs into ferromagnetic state [50,51].

Recently, a new class of 2D semiconductor, $MoSi_2N_4$ monolayer, have managed to synthesis using chemical vapor deposition (CVD) and shows unique electrical and mechanical properties [52]. The valley-dependent properties of $MoSi_2N_4$ monolayer with a pair of Dirac-type valleys have been reported, suggesting that it is a beneficial 2D material for spintronic applications [53,54]. Furthermore, it is found out that the valley polarization can be created by doping the $MoSi_2X_4$ (X = N, P, As) with V atom [55]. The high thermal conductivity of the $MoSi_2N_4$ is investigated [56]. The piezoelectricity and ferromagnetism can be induced by a small strain in the VSi_2X_4 (X = N, P) monolayer [57]. Moreover, the electronic and optical properties of the $MoSi_2N_4/MoS_2$ vdW heterostructure have been studied [58]. Furthermore, the $MoSi_2N_4/NbS_2$ and $MoSi_2N_4$/graphene vdW heterostructures exhibit a Schottky barrier height which can be modified by the interlayer distance or applied external electric field [59]. To the best of our knowledge, different computational methods have been utilized to peruse the properties of the monolayered 2DMs [60–63] but there is no any study focused on vacancy defects, adsorption of atoms, strain, and atom substitution (doping) of the $MoSi_2N_4$ monolayer.

In this paper, we modified the recently synthesized and simulated 2D $MoSi_2N_4$ MXene structure using the ab initio method. The chemisorption of F-, H- and O- adatoms on the $MoSi_2N_4$ monolayer, substitutional doping by of As, F, Ge, O, and P atoms in the low concentration range, and finally, vacancy defects created by elimination of single N and Si, or both atoms from the crystalline structure, have been studied in detail.

2. Computational methodology

The DFT calculations are performed in this work using the plane-wave basis projector augmented wave method along with the generalized gradient approximation with Perdew-Burke-Ernzerhof [64,65] functional as implemented in the Vienna *ab initio* Simulation Package [66,67]. The kinetic energy cut-off of 500 eV was set for plane-wave expansion and the energy was minimized structures are obtained until variation in the energies fall below 10^{-8} eV. To get the optimized structures, the total Hellmann–Feynman forces were reduced to 10^{-7} eV/Å. $21 \times 21 \times 1$ Γ centered k-point sampling was employed for the primitive unit cells by the Monkhorst–Pack [68]. The vacuum distance between two neighboring layers, in z direction, was 20 Å, to avoid any image interaction. Test calculations including changing the vacuum distance and the number of k points, have shown the convergence of our results. The Bader charge analysis [69] was utilized to determine the electron charge transfer, and the vibrational properties were computed

by the finite-displacement method implemented in the PHONOPY code [70]. Van der Waals correction proposed by Grimme was implemented to describe the long-range vdW interactions [71].

Adsorption energy is calculated by $E_d = E_{X@MSN} - E_X - E_{MSN}$, where $E_{X@MSN}$, E_X and E_{MSN} are the energies of H@MSN, X atom (X = H, N, O) and pristine MSN sheet, respectively. The work function, Φ, is calculated from the electrostatic potential, $\Phi = E_{vacuum} - E_F$, where E_{vacuum} is the energy of vacuum and E_F is the Fermi energy.

3. Pristine MSN monolayer

Fig. 1(a) illustrates the top and side views of the intrinsic MSN monolayer, which belongs to the hexagonal (honeycomb) lattice with the $P6m1$ space group. The side view shows that this 2D monolayer is composed of atomic layers in the order of N-Si-N-Mo-N-Si-N along the z-axis, i.e., the heavy atoms layer is sandwiched by two layers of light atoms, with a thickness of 6 Å. The MSN structural parameters have been studied in more detail in previous studies [52,9]. The dynamical stability is confirmed by calculating the phonon dispersions through the whole Brillouin zone (Fig. 1(b)). Phonon branches do not include any imaginary frequencies which mean the structure has dynamical stability. The phonon dispersion curves of $MoSi_2N_4$ contains three acoustic and sixteen optical phonon branches. Among the optical branches, eleven are found to be non-degenerate out-of-plane vibrational modes, while between remaining five there are three different double-degenerate phonon modes. For the acoustic branches, the frequency of the out-of-plane is quadratic as the frequencies go to zero. The degenerate and no-degenerate of optical branches are separated by a gap. The homopolar modes (dispersionless phonon) are located at 580, 610 and 820 cm^{-1}. The dispersionless phonons can be assigned to the SiN layers vibrating in the counter phase in the normal direction, while the MoN layers remain stationary [52,9]. The Bader charge analysis was performed to quantitatively analyze the interaction between the atoms involved in the compound. Fig. 1(c) displays the difference charge density of the MSN monolayer, where the blue and yellow colors refer to the gain charge and loss charge, respectively. The charges transfer from the positively charged atoms (Si and Mo) to the negatively charged N
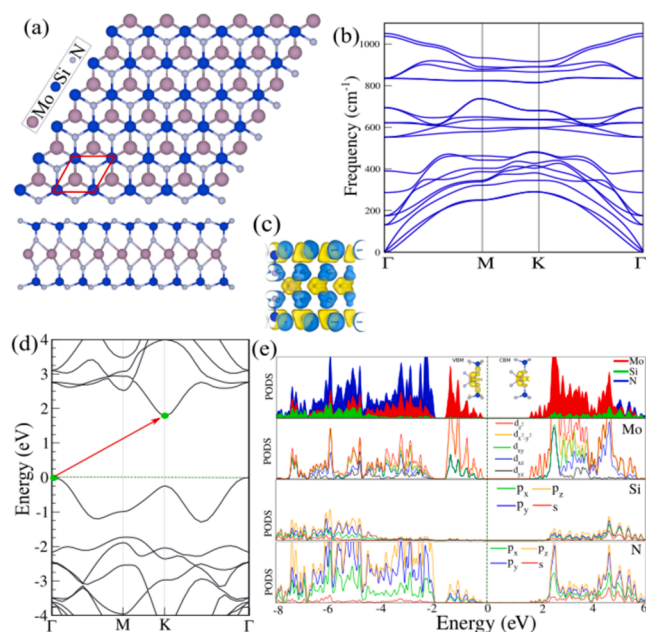

Fig. 1. (a) Top and side views of the $MoSi_2N_4$ atomic structure (the primitive unit cell is indicated by a red parallelogram), (b) phonon band dispersion, (c) The density of gain and loss charges (blue and yellow colors refer to the gain charge and loss charge, respectively), (d) electronic band structure and (e) DOS and PDOS of $MoSi_2N_4$ monolayer (the zero of energy is set to the Fermi energy).

atom (gains $\sim 2.23e$ from Si and $\sim 1.5e$ from Mo). Fig. 1(d) depicts the band structure of the MSN monolayer. Notably, it has an indirect bandgap of 1.79 eV, which is in a good agreement with the experimental value (1.94 eV) [52]. The band gap determined by means of the HSE06 is 2.35 eV [9], i.e., it overestimates the experimental value. Therefore, the PBE method is the suitable exchange correlation functional for the $MoSi_2N_4$. Furthermore, the change in the band structure using the spin–orbit coupling (SOC) is negligible (see Fig. S1, Supplementary Information). The bottom of the conduction band is located at the K-point, while the top of the valence band is located at the Γ- point. Fig. 1(e) reveals the bottom of the conduction band is contributed only by d_{z^2} Mo states with a σ(Mo-Mo) bonding. On the other hand, the top of the valence band is dominated by d_{z^2} and $d_{x^2-y^2}$ Mo states with a smaller contribution of the p_z Si and N states, representing σ(Mo-Mo) bonding hybridized with σ(N-Si) bonding.

4. Impact of different point defects

The effect of the adsorbed atom (@MSN), atomic doping (-MSN), and vacancy (V) defects on the structural, electronic and magnetic properties of the pristine MSN monolayer is investigated. With fully structural optimization, the calculations are performed using $2 \times 2 \times 1$ MSN supercell which contains 63 atoms (9 Mo, 18 Si and 36 N atoms). To obtain vacancy defects, we have removed Si (V_{Si}) or N (V_N) atoms from the MSN monolayer to produce single vacancies, while a double vacancy (V_{N+Si}) is created by removing one N and one Si atoms simultaneously. The V_N is the surface vacancy which is more likely to be of experimental relevance than the non-surface N vacancy.

4.1. Adsorption atoms effect

The electronic structure of the MSN monolayer can be modified by the adsorption of an atom on its surface. The stable sites of adsorption are calculated by placing the atom on different sites. The different adsorption sites in the MSN are the following: the top site above a Si atom (T_{Si}); the top site above N atom (T_N); the hollow site above the center of a hexagon composed of both Si and N (H_{SiN}); the bridge site above the middle of a Si-N bond (B_{SiN}). For H@MSN and O@MSN we find the most stable structure is achieved in the case of T_N and the H-N and O-N bond lengths are 1.03 and 1.44 Å, respectively. Meanwhile, the most stable structure for F@MSN is the T_{Si} configuration and the bond length of F-Si is 1.61 Å. The bond lengths of H-N, O-N, and F-Si increase as the atomic radius of adsorbed atom increases. We found out the charge transfer is $-0.44e$, $-0.56e$, and $-0.42e$ for H@MSN, O@MSN, and F@MSN systems, Fig. 2. The large charge transfer value for O@MSN as compared to the other system is related to the high electronegativity values for O and N atoms. The calculated adsorption energy is -0.25, -1.75, and -3.62 eV for H@MSN, O@MSN, and F@MSN, respectively. The computed work function for H@MSN, O@MSN, and F@MSN is: 2.83 eV, 5.58 eV, 5.97 eV, respectively. The adsorption energy and work function increase as the electronegativity of the adsorbed atom increases. The difference charge density of the MSN adsorbed with H, F and O atoms is presented in Fig. 2in the right panel), where the blue (yellow) regions represent the charge accumulation (depletion). We found that the bond formation, charge accumulation, and depletion regions can be clearly in Fig. 2. It can be seen that electrons are accumulated on the adsorbed atoms and the charge transfer is occurs from MSN monolayer to the H, F and O atoms. The charge transfer calculations show that H, F and O gain $0.44e$, $0.42e$ and $0.56e$, respectively, from the corresponding MSN adsorbed structure. These observations indicate a character of covalent bonding and chemisorption.

We now analyze the band structures, density of states (DOS) and projected DOS (PDOS) of the H@MSN, O@MSN, and F@MSN structures. In Fig. 2(a), we illustrate the band structure of the H@MSN. As compared to the band structures of the MSN sheet, Fig. 2(a), the Fermi energy is shifted towards higher energies due to the adsorption of the H atom. The system has one more electron, as compared to the pristine structure, which creates the states at the bottom of the conduction band and the structure becomes n-type conducting with a band gap of 1.75 eV. The band structure of the H@MSN is not similar to the band structure of the MSN sheet. Fig. 2(a) shows that the valence band maximum (VBM)
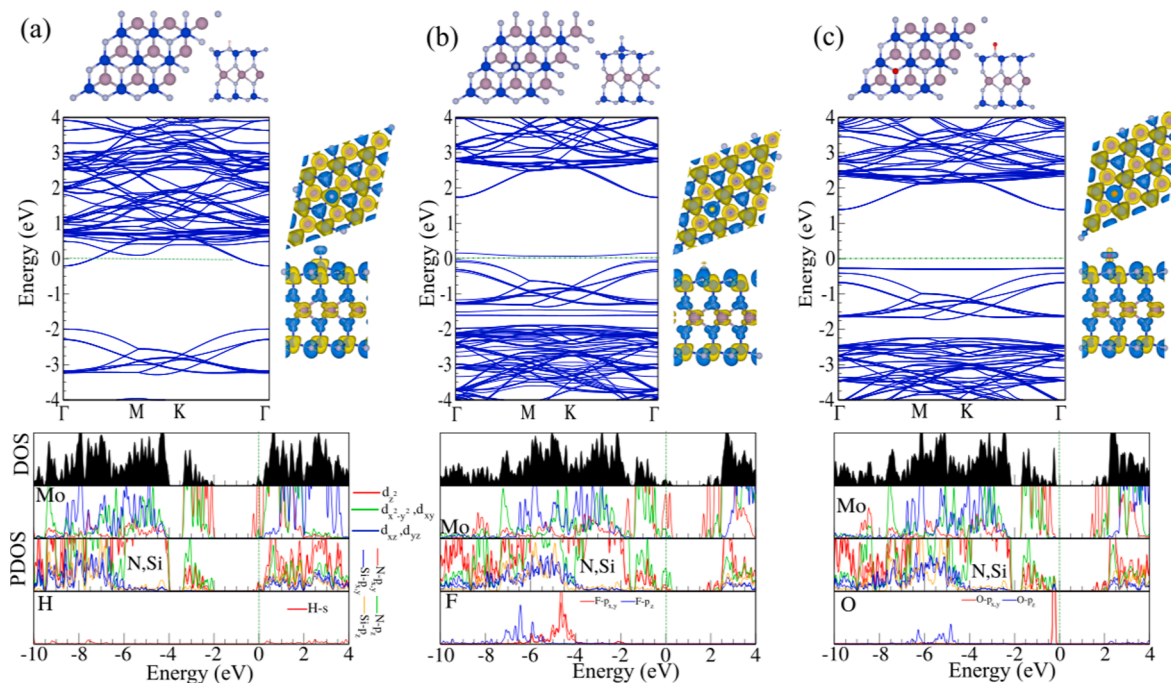
Fig. 2. Top and side views of optimized structure (up) (the grey, blue, brown, pink and red spheres refer to N, Si, Mo, H/F, and O atoms, respectively, electronic band structure (middle) and DOS/PDOS (bottom) of (a) H@MSN, (b) F@MSN and (c) O@MSN. The zero of energy is set at the Fermi energy. Difference charge densities indicated in the right panel of band structure blue and yellow colors refer to the gain charge and loss charge, respectively). (For interpretation of the references to colour in this figure legend, the reader is referred to the web version of this article.)

and conduction band minimum (CBM) are still dominated by the same states like in the case of the pristine MSN due to the very small contribution of the H state in the energy range considered. Regarding F@MSN, the Mo (d_{z^2} and $d_{x^2-y^2}$) with a small contribution of N (p_z) states are created around the Fermi level energy as compared to the MSN sheet. The contribution of F states appears in the energy range from −8 eV to −6 eV for the $p_{x,y}$ states and from −6 eV to −4 eV for the p_z states. The VBM and CBM are still dominated by Mo states and the bandgap of this structure is 1.5 eV (see Fig. 2(b)). Due to the higher electronegativity of F atom as compared to the electronegativity of and Mo, Si, and N atoms, a fluorine states perturb the spectrum due to the strong interaction, resulting in the F states falling below the valence band edge of the MSN. This will cause an electron from the MSN to occupy the lowest unoccupied molecular orbital of F atom therfore the structure is a p-type conducting. The O@MSN structure is a semiconductor with a direct band gap of 1.35 eV at the Γ- point. The VBM becomes flatter as compared to the corresponding one of the pristine, H@MSN and F@MSN. The VBM is dominated by O ($p_{x,y}$) states and the CBM is dominated by Mo states. The O states contribution appears in the energy range from −7.0 to −4.3, at top of the VB (below the Fermi energy) and in the CB at 2.1 eV. The CB is shifted towards the lower energy due to the contribution of O states. The Fermi energy is located in the gap as in the pristine structure. Therefore the type of O@MSN is a semiconductor. The gain/loss charge mapping has been plotted in Fig. 2(c). It is obvious, the charge gain of the O dopant is higher than for the others which can be attributed to the higher electronegativity of O and N atoms.

4.2. Atomic doping effect

The MoSi$_2$N$_4$ monolayer is substitutionally doped by As, Ge, and P atoms at the Si site, and by F- and O-doping at the N site. The computational results are summarized in Fig. 3. The Ge, As, and P atoms in the Ge-, As- and P-MSN, respectively, interact through sp^2-hybridization and form three σ bonds to neighboring N atoms of the MSN, inducing a notable structural deformation perpendicular to the surfaces. The calculated bond lengths of the Ge-N, As-N, and P-N are: 1.85 Å, 1.90 Åand 1.68 Å, respectively. The bond lengths and angles are dependent on the sizes of dopants and have a small effect on the planar structures due to the interaction between the sp^2-hybridization of the dopant atom with neighboring Si atoms. The calculated bond lengths of O-Si and F-Si are 1.82 and 2.25 Å, respectively. As the atomic radius of the dopant increases the bond length increases too. The formation energy (E^f) substitutional defect, where the atom X (Si or N) is replaced by the atom D, gives an indication which Y dopant is more likely to be of experimental relevance than others; it is defined as:

$E^f = E^{doped} + E^X - (E^{pristine} + E^D)$ where $E^{doped}, E^X, E^{pristine}$, and E^D refer to the total energy of MoSN with D dopant, isolated X atom, pristine structure, and isolated D atom, respectively. We determine $E^{Si}, E^{As}, E^{Ge}, E^P$ from the Si, As, Ge, and P isolated atom energy, respectively, while we assume E^N, E^O, and E^F to be the corresponding of the half the molecular energy. We find the formation energies of As-, Ge-, P-, O-, and F-MSN are −16.03 eV, −20.20 eV, −18.88 eV, −8.41 eV, and −2.24 eV, respectively. This refers to the substitutional defects in the Si site are more stable structures and Ge-MSN is the most stable one.

Now we are going to discuss the effect of dopants on the electronic structure of MSN. Fig. 3(a) shows that the As-MSN has a magnetic moment due to the asymmetric DOS for two spin components. We find the magnetic moment is 1 μ_B because As has one more electron in the outer shell as compared to Si. The midgap states for the spin up component are created close to the Fermi energy. The As atom states are dominated at 0.25 eV for the spin down component and in this midgap states. This structure can be considered as a half-metallic (dilute-magnetic semiconductor). Computational results regarding doping at the N site are illustrated in Fig. 3(b). Obviously, the structure is a semiconductor with an indirect band gap. We have determined the band gap is 1.25 eV and the F states have contributions at the bottom of the CB and at the top of the VB. Fig. 3(c) shows that the Ge-doped MSN is a semiconductor with a band gap of 1.75 eV. The VBM and CBM are still dominated by Mo states. The Ge states have good contributions inside the VB and CB. For O-doped MSN, the band structure is very similar to the band structure of P-doped MSN with the same band gap and n-type conducting behavior (see Fig. 3(d)). For P-doped MSN, Fig. 3(e), the Fermi energy is shifted towards the higher energies and the P dopant creates states around the Fermi energy so, the structure becomes n-type conducting with a band gap of 1.75 eV. The bottom of the CB is dominated by Mo states with a small portion of P states, while the VB is dominated by Mo states only. The P states have a larger contribution to the VB than to the CB. The difference charge density of the MSN doped with As, F, Ge, O and P) is presented in Fig. 3(f). The blue and yellow regions represent the charge accumulation and depletion, correspondingly. Notice that the bond formation, charge accumulation, and depletion regions can be clearly seen in Fig. 3(f). It can be seen that electrons are depleted on the As and Ge dopants, whereas the majority of electron enhancement has shown the charge transfer from As and Ge doping atoms to the MSN monolayer. The charge transfer calculations show that As, Ge and P lose 1.72 e, 1.9 e, and 3.22 e, respectively, while O and F gain 1.64 e and 0.77 e, respectively, from the surrounding atoms of the corresponding MSN doped structure. These observations indicate a character of covalent bonding and chemisorption. The calculated work function value is 5.19 eV, 4.09 eV, 3.17 eV, 3.12 eV, 5.23 eV for Ge-, As-,
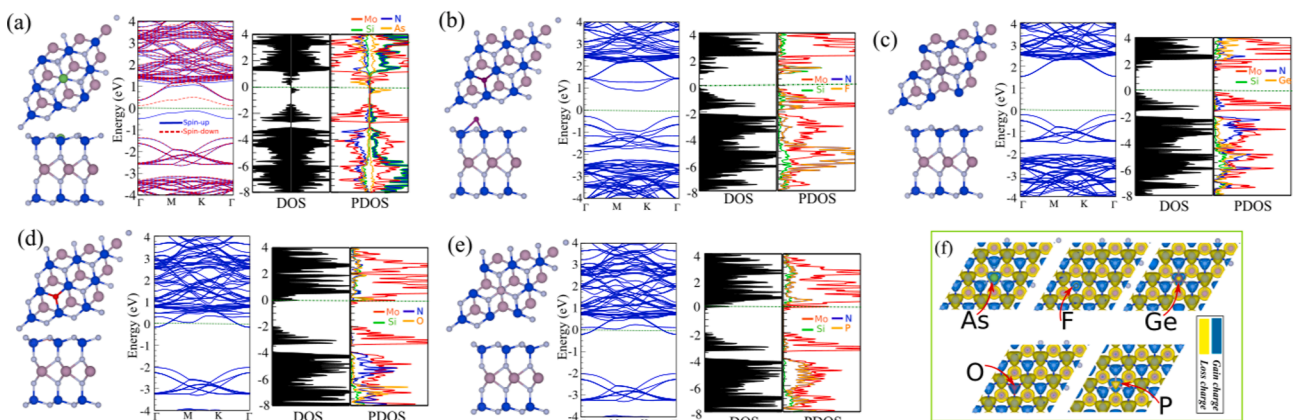

Fig. 3. Top and side views of optimized structure (left), electronic band structure (middle) and DOS/PDOS (right) of doped-MSN: (a) As-MSN atom, (b) F-MSN, (c) Ge-MSN, (d) O-MSN, and (e) P-MSN. (f) Difference charge densities of the studied structures with isosurface value of 0.003 e/Å^3. The zero of energy is set at the Fermi energy.

P-, O-, and F-MSN structures, respectively.

4.3. Vacancy defects

Next we explore the effect of vacancy defects such as V_{Si}, V_N, V_{N+Si} and V_{Mo} on the MSN properties. The Ab initio molecular dynamics (AIMD) simulation of the MoSi$_2$N$_4$ monolayer with a single N vacancy, as an example, shows that the structure could stay intact at 500 K with a very stable energy and temperature profiles, indicating the thermal stability of the MSN monolayer with a N vacancy (see Figs. S2(a-c), Supplementary Information). The computed optimized atomic structures with the corresponding electronic band structure of vacancies are demonstrated in Figs. 4(a-c). We discover that the Si and N atoms around the vacancy do not undergo a Jahn–Teller distortion [72]. Notice also the non-reconstructed MSN structures in the presence of the considered types of vacancies. The calculated bond lengths of N-Si and Mo-N at the edge of V_{Si} are 1.74 Å. and 2.08 Å, respectively. The computed work function value is 4.36 eV, which is smaller than the work function value of the pristine MSN (5.12 eV) [52,9]. The formation energy (E^f) gives an indication which Y vacancy is more likely to be of experimental relevance than others; it is defined as: $E^f = E^{vacancy} + E^Y - E^{pristine}$, where $E^{vacancy}$, E^Y and $E^{pristine}$ refer to the total energy of MoSN with Y vacancy, isolated Y atom, and of pristine structure, respectively. We determine $E^{Mo(Si)}$ from the Mo (Si) isolated atom energy, while we assume E^N to be half the molecular energy. We have determined the formation energies of V_{Si}, V_N, V_{N+Si}, and V_{Mo} are 24.27 eV, 11.34 eV, 12.15 and 16.15 eV, respectively. This means that the V_N is by far the most stable vacancy defect among the ones considered, followed by the V_{N+Si}, V_{Mo}, and V_{Si} defects.

Clearly, the V_{Si} creates states at the Fermi level for the spin up component only. These states are dominated by Si and N states, see the Supplementary Information (Fig. S1(a)). Because of the asymmetric DOS for the two spin components, the structure has a magnetic moment of 1 μ_B. This structure can be considered as a half-metallic and it is promissing for spintronic applications (see Fig. 4(a)) due to the metallic state at the Fermi energy for one spin component [73].

Fig. 4(b), exhibit the band structure of the MSN with V_N (V_N-MSN). The average bond lengths of N-Si and Mo-N at the edge of V_{Si} are 1.74 Åand 2.08 Å, respectively, which are very similar to the corresponding bond lengths in the case of V_{Si}-MSN. The work function value becomes 6.01 eV which is larger than the corresponding one of pristine and V_{Si}-MSN due to the metallicity of the V_N-MSN system. The asymmetry between the spin up and spin down in the band structure induces a magnetic moment of $\sim$ 1 μ_B. The Mo states are dominant for the spin up

component, while the N and Mo states are dominant for the spin down component at the Fermi energy (see Fig. S1(a)). Due to the asymmetry of the two spin orientations at the Fermi energy, this system can be used in spin filter applications [74]. The last defective structure within the studied configurations includes the double vacancy (V_{Si+N}). The bond lengths of N-Si and Mo-N are very similar to the corresponding bond lengths in the case of the V_N-MSN structure. The work function is 6.23 eV which is the largest value in this study indicating the metallicity character of the V_{Si+N}-MSN structure. The band structure, represented in Fig. 4(c) is also similar to the corresponding one of the V_N-MSN structure with higher concentration of N and Mo states at the Fermi energy (for spin down component, Fig. S1(c)). The magnetic moment is determined as $\sim$ 2 eV due to the effect of the double vacancy. Therefore, the V_{Si+N}-MSN structure could be beneficial for spin filter devices. Regarding the last vacancy in this study, V_{MO}, the created states at 0.5 eV and 1.2 eV decrease the band gap to 0.65 eV as compared to the bandgap of the pristine structure (Fig. 4(d)). The Mo states are dominated in the created states with a good contribution from Si states (Fig. S3(d), Supplementary Information). The V_{Mo}-MSN is a non-magnetic structure. In order to analyze the magnetism, the difference spin density of the MSN monolayer with different vacancy defects is illustrated in Fig. 4(e). The blue and yellow regions represent the ↑ and ↓ spin channels, respectively. The difference spin density is calculated from the difference spin density between ↑ and ↓ spin channels. One can conclude that the magnetism mainly originates from the vacancy atoms in the MSN monolayer.

5. Conclusion

In summary, employing spin-polarized DFT, the effect of different types of point defects on the structural, electronic and magnetic properties of MoSi$_2$N$_4$ monolayer has been investigated. We considered H, O, and F as adsorbed atoms, As, Ge, P as substitutionally doped atoms at Si site, and O and F as substitutional doped atoms at N site, and Si, N, and Si + N vacancies in this study. The structures of the H@MSN, O-MSN, P-MSN are n-type conducting due to the created states at the bottom of the conduction band. The As doped MSN, and defected structures with the considered vacanciesy have a magnetic moment. The V_{Si}-MSN structure is half-metallic and can be used in spintronic applications, while the V_N- and V_{Si+N}-MSN structures are metallic and they can be employed in spin filter devices.
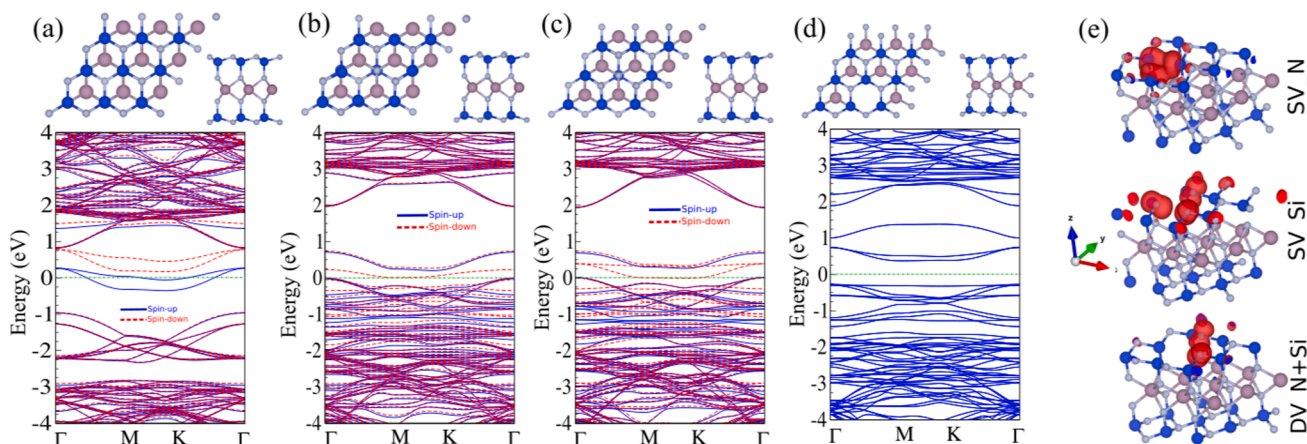
Fig. 4. Optimized atomic structures with corresponding electronic band structure of MoSi$_2$N$_4$ monolayer with (a) single N vacancy, (b) single Si vacancy, (c) N + Si vacancies, and (d) single Mo vacancy defects. (e) Difference spin densities of the (a-c) studied structures. The blue and yellow regions represent the ↑ and ↓ spin channels, respectively. The zero of energy is set to Fermi-level. (For interpretation of the references to colour in this figure legend, the reader is referred to the web version of this article.)

Declaration of Competing Interest

The authors declare that they have no known competing financial interests or personal relationships that could have appeared to influence the work reported in this paper.

Acknowledgment

Appendix A. Supplementary material

Supplementary data associated with this article can be found, in the online version, at https://doi.org/10.1016/j.apsusc.2021.149862.

References

[1] K.S. Novoselov, A.K. Geim, S.V. Morozov, D. Jiang, Y. Zhang, S.V. Dubonos, I.V. Grigorieva, A.A. Firsov, Electric Field Effect in Atomically Thin Carbon Films. Sci. 306, 666 (2004).

[2] K.S. Novoselov, D. Jiang, F. Schedin, T.J. Booth, V.V. Khotkevich, S.V. Morozov, A. K. Geim, Two-Dimensional Atomic Crystals, Proc. Natl. Acad. Sci. 102 (2005) 10451.

[3] X. Huang, M. Leng, W. Xiao, M. Li, J. Ding, T.L. Tan, W.S.V. Lee, J. Xue, Activating Basal Planes and S-Terminated Edges of MoS$_2$ toward More Efficient Hydrogen Evolution, Adv. Func. Mater. 27 (2017) 1604943.

[4] K.S. Novoselov, Q. Ge, D.V. Andreeva, Grinding Exfoliation for Scalable Production of 2D Materials, Natl. Sci. Rev. 7 (2020) 559.

[5] F. Bonaccorso, L. Colombo, G. Yu, M. Stoller, V. Tozzini, A.C. Ferrari, R.S. Ruo, V. Pellegrini, Graphene, related two-dimensional crystals, and hybrid systems for energy conversion and storage, Science 347 (2015) 6217.

[6] Q. Chen, Q. Ding, Y. Wang, Y. Xu, J. Wang, Electronic and Magnetic Properties of Two Dimensional Transition-Metal Phosphorous Chalcogenides TMPS$_4$, J. Phys. Chem. C 124 (2020) 12075.

[7] M. Xu, C. Huang, Y. Li, S. Liu, X. Zhong, P. Jena, E. Kan, Y. Wang, Electrical Control of Magnetic Phase Transition in a Type-I Multiferroic Double-Metal Trihalide Monolayer, Phys. Rev. Lett. 124 (2020) 067602.

[8] X.L. Wei, Z.K. Tang, G.C. Guo, S. Ma, L.M. Liu, Electronic and magnetism properties of two-dimensional stacked nickel hydroxides and nitrides, Sci. Rep. 5 (2015) 11656.

[9] A. Bafekry, M. Faraji, D.M. Hoat, M.M. Fadlallah, M. Shahrokhi, F. Shojaei, D. Gogova, M. Ghergherehchi, MoSi$_2$N$_4$ single-layer: a novel two-dimensional material with outstanding mechanical, thermal, electronic and optical, J. Phys. D Appl. Phys. 54 (2021) 155303.

[10] J. Zhang, Y. Yu, P. Wang, C. Luo, X. Wu, Z. Sun, J. Wang, W.D. Hu, G. Shen, Characterization of atomic defects on the photoluminescence in two-dimensional materials using transmission electron microscope, InfoMat. 1 (2019) 85.

[11] A. Bafekry, S. Farjami Shayesteh, F.M. Peeters, Introducing novel electronic and magnetic properties in C$_3$N nanosheets by defect engineering and atom substitution, Phys. Chem. Chem. Phys. 21 (2019) 21070.

[12] A.K. Geim, I.V. Grigorieva, Van der Waals heterostructures, Nat. 499 (2013) 419.

[13] A. Celis, M.N. Nair, A. Taleb-Ibrahimi, E.H. Conrad, C. Berger, W.A. de Heer, A. Tejeda, Graphene nanoribbons: fabrication, properties and devices, J. Phys. D Appl. Phys. 49 (2016) 143001.

[14] M. Srivastava, A. Srivastava, S.K. Pandey, Suitability of Graphene Monolayer as Sensor for Carcinogenic Heavy metals in Water: A DFT Investigation, Appl. Surf. Sci. 517 (2020) 146021.

[15] B. Chilukuri, U. Mazur, K.W. Hipps, Structure, Properties, and Reactivity of Porphyrins on Surfaces and Nanostructures with Periodic DFT Calculations, Appl. Sci. 10, 740 (2020).

[16] Z. Lin, B.R. Carvalho, E. Kahn, R. Lv, R. Rao, H. Terrones, M.A. Pimenta, M. Terrones, dichalcogenides, 2D Mater. 3, 022002 (2016).

[17] D. Yang, X. Fan, F. Zhang, Y. Hu, Z. Luo, Electronic and Magnetic Properties of Defected Monolayer WSe$_2$ with Vacancies, Nanoscale Res. Lett. 14 (2019) 192.

[18] X. Wang, Y. Zhang, H. Si, Q. Zhang, J. Wu, L. Gao, X. Wei, Y. Sun, Q. Liao, Z. Zhang, K. Ammarah, L. Gu, Z. Kang, Y. Zhang, Single-Atom Vacancy Defect to Trigger High-Efficiency Hydrogen Evolution of MoS$_2$, J. Am. Chem. Soc. 142 (2020) 4298.

[19] X.D. Duan, C. Wang, A.L. Pan, R.Q. Yu, X.F. Duan, Two-dimensional transition metal dichalcogenides as atomically thin semiconductors: opportunities and challenges, Chem. Soc. Rev. 44 (2015) 8859.

[20] F. Gong, W. Luo, J. Wang, P. Wang, H. Fang, D. Zheng, N. Guo, J. Wang, M. Luo, J. C. Ho, X. Chen, W. Lu, L. Liao, W. Hu, High-sensitivity floating-gate phototransistors based on WS$_2$ and MoS$_2$, Adv. Funct. Mater. 26 (2016) 6084.

[21] D. Jariwala, V.K. Sangwan, L.J. Lauhon, T.J. Marks, M.C. Hersam, Emerging device applications for semiconducting two-dimensional transition metal Dichalcogenides, ACS Nano. 8 (2014) 1102.

[22] L. Vicarelli, S.J. Heerema, C. Dekker, H.W. Zandbergen, Controlling Defects in Graphene for Optimizing the Electrical Properties of Graphene Nanodevices, ACS Nano 9 (2015) 3428.

[23] M.T. Lusk, L.D. Carr, Nanoengineering Defect Structures on Graphene, Phys. Rev. Lett. 100 (2008) 175503.

[24] K. Sevim, H. Sevincli, Structural, electronic, and magnetic properties of point defects in polyaniline (C$_3$N) and graphene monolayers: A comparative study, J. Appl. Phys. 127 (2020) 195102.

[25] A. Bafekry, C. Stampfl, M. Ghergherehchi, S.F. Shayesteh, A first-principles study of the effects of atom impurities, defects, strain, electric field and layer thickness on the electronic and magnetic properties of the C$_2$N nanosheet, Carbon 157 (2020) 371–384.

[26] A. Kasry, M.M. Fadlallah, N.H. Voelcker, A.A. Maarouf, Experimental and Theoretical Demonstrations of Ultraviolet Absorption Enhancement in Porous Nano-Membrane Graphene, Carbon 155 (2019) 65.

[27] S. Bertolazzi, D. Krasnozhon, A. Kis, Nonvolatile memory cells based on MoS$_2$/ Graphene Heterostructures, ACS Nano. 7 (2013) 3246.

[28] J. Jiang, T. Xu, L. Lu, Z. Ni Sun, Defect engineering in 2D materials: Precise manipulation and improved functionalities, Research (2019, 2019,) 4641739.

[29] A. Bafekry, C. Stampfl, B. Akgenc, B. Mortazavi, M. Ghergherehchi, Ch.V. Nguyen, Embedding of atoms into the nanopore sites of the C$_6$N$_6$ and C$_6$N$_8$ porous carbon nitride monolayers with tunable electronic properties, Phys. Chem. Chem. Phys. 22 (2020) 6418–6433.

[30] A. Bafekry, C. Stampfl, B. Akgenc, M. Ghergherehchi, Control of C$_3$N$_4$ and C$_4$N$_3$ carbon nitride nanosheets' electronic and magnetic properties through embedded atoms, Phys. Chem. Chem. Phys. 22 (2020) 2249–2261.

[31] S. Wang, A. Robertson, J.H. Warner, Atomic structure of defects and dopants in 2D layered transition metal dichalcogenides, Chem. Soc. Rev. 47 (2018) 6764.

[32] D. Rhodes, S.H. Chae, R. Ribeiro-Palau, J. Hone, Disorder in van der Waals heterostructures of 2D materials, Nat. Mater. 18 (2019) 541.

[33] Z. Wu, Z. Luo, Y. Shen, W. Zhao, W. Wang, H. Nan, X. Guo, L. Sun, X. Wang, Y. You, Z. Ni, Defects as a factor limiting carrier mobility in WSe$_2$: A spectroscopic investigation, Nano Res. 9 (2016) 3622.

[34] M.R. Rosenberger, H.J. Chuang, K.M. McCreary, C.H. Li, B.T. Jonker, Electrical characterization of discrete defects and impact of defect density on photoluminescence in monolayer WS$_2$, ACS Nano 12 (2018) 1793.

[35] A. Bafekry, C. Nguyen, C. Stampfl, B. Akgenc, M. Ghergherehchi, Oxygen Vacancies in the Single Layer of Ti$_2$CO$_2$ MXene: Effects of Gating Voltage, Mechanical Strain, and Atomic Impurities, physica status solidi (b) 257 (12), 2000343 (2020).

[36] H. Qiu, T. Xu, Z. Wang, W. Ren, H. Nan, Z. Ni, Q. Chen, S. Yuan, F. Miao, F. Song, G. Long, Y. Shi, L. Sun, J. Wang, X. Wang, Hopping transport through defect-induced localized states in molybdenum disulfide, Nat. Commun. 4 (2013) 2642.

[37] J. Hong, Z. Hu, M. Probert, K. Li, D. Lv, X. Yang, L. Gu, N. Mao, Q. Feng, L. Xie, J. Zhang, D. Wu, Z. Zhang, C. Jin, W. Ji, X. Zhang, J. Yuan, Z. Zhang, Exploring atomic defects in molybdenum disulphide monolayers, Nat. Commun. 6 (2015) 6293.

[38] E. Liu, M. Long, J. Zeng, W. Luo, Y. Wang, Y. Pan, W. Zhou, B. Wang, W. Hu, Z. Ni, Y. You, X. Zhang, S. Qin, Y. Shi, K. Watanabe, T. Taniguchi, H. Yuan, H.Y. Hwang, Y. Cui, F. Miao, D. Xing, High responsivity phototransistors based on few-layer ReS$_2$ for weak signal detection, Adv. Funct. Mater. 26 (2016) 1938.

[39] J. Shim, A. Oh, D.H. Kang, S. Oh, S.K. Jang, J. Jeon, M.H. Jeon, M. Kim, C. Choi, J. Lee, S. Lee, G.Y. Yeom, Y.J.e Song, J.H. Park, High-performance 2D rhenium disulfide (ReS$_2$) transistors and photodetectors by oxygen plasma treatment, Adv. Mater. 28 (2016) 6985.

[40] Z. Hu, Z. Wu, C. Han, J. He, Z. Ni, W. Chen, Two-dimensional transition metal dichalcogenides: interface and defect engineering, Chem. Soc. Rev. 47 (2018) 3100.

[41] A. Bafekry, M. Yagmurcukardes, M. Shahrokhi, M. Ghergherehchi, Electro-optical properties of monolayer and bilayer boron-doped C$_3$N: Tunable electronic structure via strain engineering and electric field, Carbon 168 (2020) 220–229.

[42] A. Bafekry, M. Shahrokhi, M. Yagmurcukardes, D. Gogova, M. Ghergherehchi, B. Akgenc, S.A.H. Feghhi, Surface Functionalization of the Honeycomb Structure of Zinc antimonide (ZnSb) Monolayer: a First-Principles study, Surf. Sci. 707 (2021) 121796.

[43] A. Bafekry, D. Gogova, M.M. Fadlallah, C. Nguyen, M. Ghergherehchi, M. Faraji, S. A.H. Feghhi, M. Oskoeian, Electronic and Optical Properties of Two-Dimensional Heterostructures and Heterojunctions between Doped-Graphene and C-and N-containing Materials, Phys. Chem. Chem. Phys. 23 (2021) 4865.

[44] Y. Kadioglu, F. Ersan, D. Kecik, O.U. Akturk, E. Akturk, S. Ciraci, Chemical and substitutional doping, and anti-site and vacancy formation in monolayer AlN and GaN, Phys. Chem. Chem. Phys. 20 (2018) 16077.

[45] Y. Kadioglu, S.B. Kilic, S. Demirci, O.U. Akturk, E. Akturk, S. Ciraci, Modification of electronic structure, magnetic structure, and topological phase of bismuthene by point defects, Phys. Rev. B 96 (2017) 245424.

[46] R. Singh, Peter Kroll, Magnetism in graphene due to single-atom defects: dependence on the concentration and packing geometry of defects, J. Phys.: Condens. Matter 21 (2009) 196002.

[47] H.L. Shi, H. Pan, Y.W. Zhang, B.I. Yakobson, Strong ferromagnetism in hydrogenated monolayer MoS$_2$ tuned by strain, Phys. Rev. B 88 (2013) 5326.

[48] H.Y. Song, J.T. Lu, Single-site point defects in semimetal WTe$_2$: A density functional theory study, AIP Adv. 8 12 (2018) 125323.

[49] P. Tao, H.H. Guo, T. Yang, Z.D. Zhang, Strain-induced magnetism in MoS$_2$ monolayer with defects, J. Appl. Phys. 115 (2014) 054305.

[50] S.X. Yang, C. Wang, H. Sahin, H. Chen, Y. Li, S.S. Li, A. Suslu, F.M. Peeters, Q. Liu, J.B. Li, S. Tongay, Tuning the optical, magnetic, and electrical properties of ReSe$_2$ by nanoscale strain engineering, Nano Lett. 15 (2015) 1660.

[51] Y. Yang, X.L. Fan, R. Pan, W.J. Guo, First-principles investigations of transition-metal doped bilayer WS$_2$, Phys. Chem. Chem. Phys. 18 (2016) 10152.

[52] Y.L. Hong, Z. Liu, L. Wang, T. Zhou, W. Ma, C. Xu, S. Feng, L. Chen, M.L. Chen, D. M. Sun, X.Q. Chen, H.M. Cheng, W. Ren, Chemical vapor deposition of layered two-dimensional MoSi$_2$N$_4$ materials, Science 369 (2020) 670.

[53] S. Li, W. Wu, X. Feng, S. Guan, W. Feng, Y. Yao, S.A. Yang, Valley-dependent properties of monolayer MoSi$_2$N$_4$, WSi$_2$N$_4$, and MoSi$_2$As$_4$, Phys. Rev. B 102 (2020) 235435.

[54] C. Yang, Z. Song, X. Sun, J. Lu, Valley pseudospin in monolayer MoSi$_2$N$_4$, and MoSi$_2$As$_4$, Phys. Rev. B 103 (2021) 035308.

[55] H. Ai, D. Liu, J. Geng, S. Wang, K.H. Lo, H. Pan, Theoretical evidence of the spinvalley coupling and valley polarization in two-dimensional MoSi$_2$X$_4$ (X = N, P, and As), Phys. Chem. Chem. Phys. 23 (2021) 3144.

[56] Yu. Jihai, J. Zhou, X. Wan, Q. Li, High intrinsic lattice thermal conductivity in monolayer MoSi$_2$N$_4$, New J. Phys. 23 (2021) 033005.

[57] S.-D. Guo, W.-Q. Mu, Y.-T. Zhu, X.-Q. Chen, Coexistence of intrinsic piezoelectricity and ferromagnetism induced by small biaxial strain in septuple-atomic-layer VSi$_2$P$_2$, Phys. Chem. Chem. Phys. 22 (2020) 28359.

[58] A. Bafekry, M. Faraji, A. Abdollahzadeh, M.M. Fadlallah, C. Nguyen, M. Ghergherehchi, S.A.H. Feghhi, Van der Waals heterostructure of MoS$_2$MoSi$_2$N$_4$: A First-principle study, New J. Chem. (2021), https://doi.org/10.1039/D1NJ00344E.

[59] L. Cao, Q. Wang, L.K. Ang, Y.S. Ang, Two-dimensional van der Waals electrical contact to monolayer MoSi$_2$N$_4$, Appl. Phys. Lett. 118 (2021) 013106.

[60] A. Bafekry, S. Farjami Shayesteh, F.M. Peeters, C$_3$N Monolayer: Exploring the Emerging of Novel Electronic and Magnetic Properties with Adatom Adsorption, Functionalizations, Electric field, Charging and Strain, J. Phys. Chem. C. 123 (2019) 12485.

[61] A. Bafekry, M. Ghergherehchi, F.M. Peeters, Adsorption of molecules on C$_3$N nanosheet: A first-principles calculations, Chem. Phys. 526 (2019) 110442.

[62] Y. Kadioglu, F. Ersan, G. Gokoglu, O.U. Akturk, E. Akturk, Adsorption of Alkali and Alkaline-Earth Metal Atoms on Stanene: A First-Principles Study, Mater. Chem. Phys. 180 (2016) 326.

[63] A. Bafekry, M. Ghergherehchi, S. Farjami Shayesteh, Tuning the electronic and magnetic properties of antimonene nanosheets via point defects and external fields: first principles calculations, Phys. Chem. Chem. Phys. 21 (2019) 10552.

[64] J.P. Perdew, K. Burke, M. Ernzerhof, Generalized gradient approximation made simple, Phys. Rev. Lett. 77 (1996) 3865.

[65] J.P. Perdew, K. Burke, M. Ernzerhof, Generalized gradient approximation made simple, Phys. Rev. Lett. 78 (1997) 1396.

[66] G. Kresse, J. Hafner, Ab initio molecular dynamics for liquid metals, Phys. Rev. B 47 (1993) 558.

[67] G. Kresse, J. Hafner, Efficient iterative schemes for ab initio total-energy calculations using a plane-wave basis set, Phys. Rev. B 49 (1994) 14251.

[68] H.J. Monkhorst, J.D. Pack, Special points for Brillouin-zone integrations, Phys. Rev. B 13 (1976) 12.

[69] G. Henkelman, A. Arnaldsson, H. Jonsson, A fast and robust algorithm for Bader decomposition of charge density, Comput. Mater. Sci. 36 (2006) 354.

[70] D. Alfe, PHON: A program to calculate phonons using the small displacement method, Comput. Phys. Commun. 180 (2009) 2622.

[71] S.J. Grimme, Semiempirical GGA-type density functional constructed with a long-range dispersion correction, Comput. Chem. 27 (2006) 1787.

[72] H.A. Jahn, E. Teller, Stability of Polyatomic Molecules in Degenerate Electronic States- I-Orbital Degeneracy, Proc. Royal Soc. London A: Mathematical, Phys. Eng. Sci. 161 (1937) 220.

[73] M.M. Fadlallah, U. Eckern, Electronic and optical properties of metal-doped TiO$_2$ nanotubes: spintronic and photocatalytic applications, N.J. Phy. 22 (2020) 093028.

[74] M.M. Fadlallah, A.A. Maarouf, U. Schwingenschlogl, U. Eckern, Unravelling the interplay of geometrical, magnetic and electronic properties of metal-doped graphene nanomeshes, J. Phys.s: Cond. Matter 29 (2016) 055301.